Electronic Supplementary Material (ESI) for Chemical Science.

Supporting information for: Controlling Destructive Quantum Interference in Tunneling Junctions Comprising Self-assembled Monolayers via Bond Topology and Functional Groups

Yanxi Zhang,[†,‡,¶] Gang Ye,[†,‡,¶] Saurabh Soni,[†,‡] Xinkai Qiu,[†,‡] Theodorus L. Krijger,[†,‡] Harry T. Jonkman,[‡] Marco Carlotti,[†,‡] Eric Sauter,[§] Michael Zharnikov,[§] and Ryan C. Chiechi[*,†,‡]

†*Stratingh Institute for Chemistry, University of Groningen, Nijenborgh 4, 9747 AG Groningen, The Netherlands*

‡*Zernike Institute for Advanced Materials, Nijenborgh 4, 9747 AG Groningen, The Netherlands*

¶*These authors contributed equally to this work.*

§*Applied Physical Chemistry, Heidelberg University, Im Neuenheier Feld 253, Heidelberg 69120, Germany*

E-mail: r.c.chiechi@rug.nl

Contents

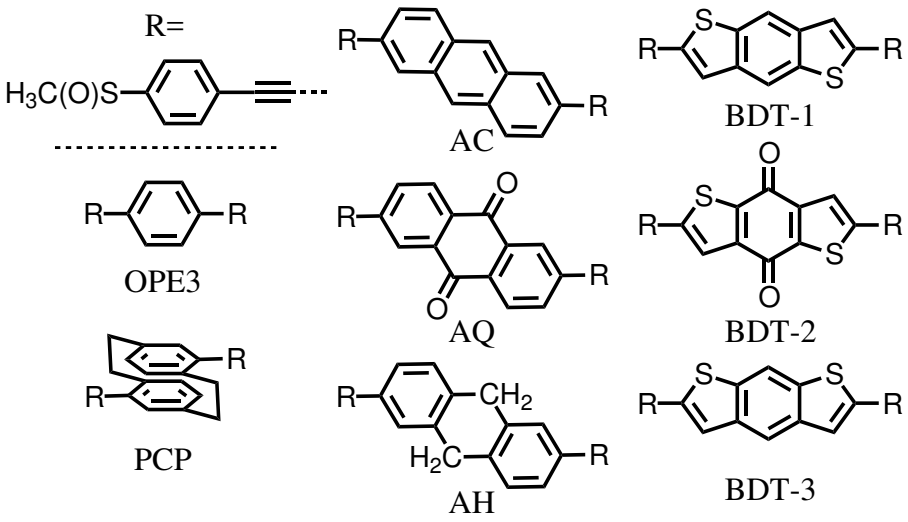

Figure S1: Structure and labels for all compounds mentioned in the main text.

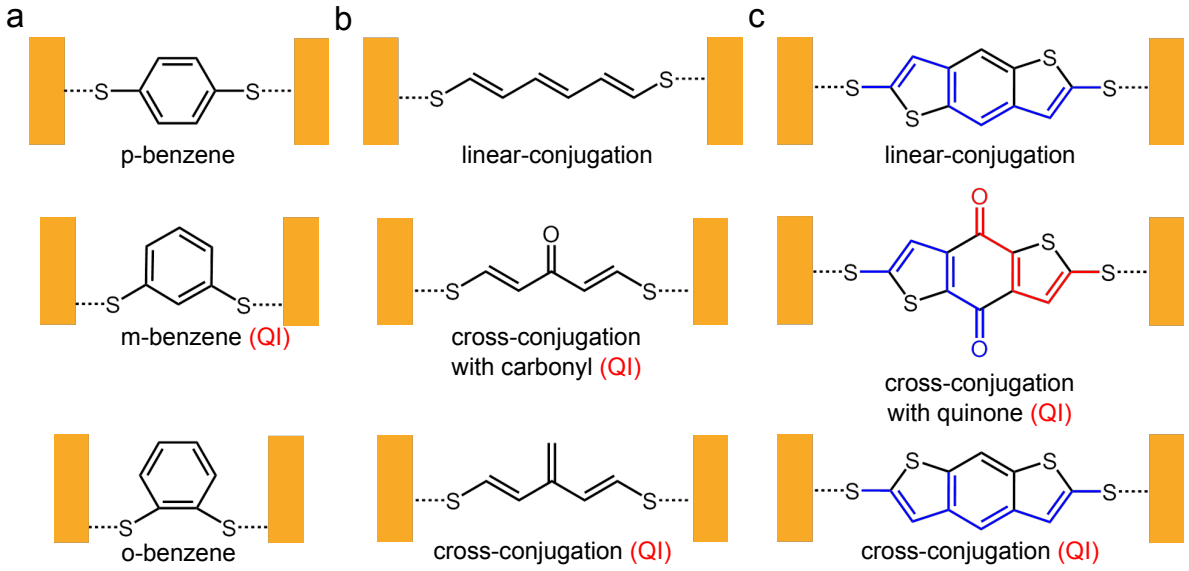

Figure S2: A schematic shows a) charge transfer through para-, meta, ortho-benzene between two electrodes (yellow rectangles). The conductance of m-benzene is lower than p- and o-benzene due to QI effects. b) charge transfer through linear-conjugation pattern of unsaturated carbon which has the same topology as AC and BDT-1, cross-conjugation pattern via carbonyl which has the same topology as AQ and BDT-2 and cross-conjugation pattern which has the same topology as BDT-3. Both cross-conjugation patterns exhibit QI effects. c) charge transfer through the core of BDT-1 which is linear-conjugated, the core of BDT-2 which is cross-conjugated with quinone and the core of BDT-3 which is cross-onjugated.

Table S1: Summary of compounds reported to exhibit quantum interference experimentally

Compound	**Technique**	**Reference**
BDT-2,3	EGaIn	This work
AQ	EGaIn, CP-AFM, MC/STM-BJ, e-Carbon	S1–S5
AH	EGaIn,MCBJ	S6,S7
PCP	EGaIn,STM	S6,S8
Azulene	STM-BJ,MCBJ	S9,S10
m-benzene/fluorene	MC/STM-BJ	S11–S19

1 Experimental

1.1 Synthesis and Characterization

Reagents. All reagents and solvents were commercial and were used as received. Benzo[1,2-b;4,5-b']dithiophene was purchased from TCI. 2,6-dibromobenzo[1,2-b:4,5-b']dithiophene-4,8-dione[S20], 2,6-dibromobenzo[1,2-b:5,4-b']dithiophene[S21], 4-ethynyl-1-thioacetylbenzene[S22] and 1-tert-butylthio-4-ethynylbenzene[S23] were synthesized according to literature procedures.

NMR and Mass Spectra. ^{1}HNMR and ^{13}CNMR were performed on a Varian Unity Plus (400 MHz) instrument at 25 °C, using tetramethylsilane (TMS) as an internal standard. NMR shifts are reported in ppm, relative to the residual protonated solvent signals of $CDCl_3$ (δ = 7.26 ppm) or at the carbon absorption in $CDCl_3$ (δ = 77.0 ppm). Multiplicities are denoted as: singlet (s), doublet (d), triplet (t) and multiplet (m). High Resolution Mass Spectroscopy (HRMS) was performed on a JEOL JMS 600 spectrometer.

General. Unless stated otherwise, all crude compounds were isolated by bringing the reaction to room temperature, extracting with CH_2Cl_2, washing with saturated $NaHCO_3$, water and then brine. The organic phase was then collected and dried over Na_2SO_4 and the solvents removed by rotary evaporation.

1.1.1 Synthesis of BDT-1

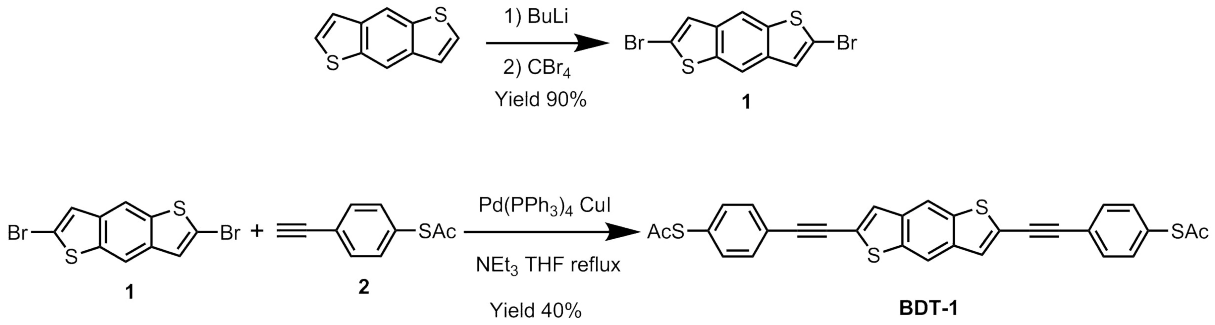

Figure S3: Synthetic route for **BDT-**1

2,6-dibromobenzo[1,2-b:4,5-b']dithiophene (1). Benzo[1,2-b;4,5-b']dithiophene (540 mg, 2.84 mmol) were dissolved in 70 mL anhydrous THF under an atmosphere of N_2, cooled to −78 °C and *n*-butyllithium (8.5 mmol, 5.3 mL, 1.6 M in hexane) was added drop-wise. The solution was stirred for 30 min in the cold bath before being warmed to room temperature and stirred for and additional 20 min. The mixture was cooled to −78 °C again and a solution of CBr_4 (2.8 g, 8.5 mmol) in 5 mL anhydrous THF was added. The solution was stirred for 30 min in the cold bath before being quenched with concentrated sodium bicarbonate solution (10 mL) at −78 °C. The crude solid was purified by recrystallization from $CHCl_3$ to give **1** (890 mg, 90 %) as colorless platelets. ^{1}HNMR (400 MHz, $CDCl_3$) δ: 8.03 (s, 2H); 7.33 (s, 2H). ^{13}CNMR (100 MHz, $CDCl_3$) δ: 138.36, 136.88, 125.63, 116.00, 115.10.

2,6-Bis[(4-acetylthiophenyl)ethynyl]benzo[1,2-b:4,5-b']dithiophene (BDT-1**).** 2,6-dibromobenzo[1,2-b:4,5-b']dithiophene (125 mg, 0.36 mmol) and 4-ethynyl-1-thioacetylbenzene (176 mg, 1 mmol) were dissolved in mixture of fresh distilled Et_3N (5 mL) and anhydrous THF (10 mL). After degassing with dry N_2, the catalysts $Pd(PPh_3)_4$ (58 mg, 0.05 mmol) and CuI (10 mg, 0.05 mmol) were added. The reaction mixture was refluxed overnight under N_2. The crude solid was purified by column chromatography to give **BDT-**1 (78 mg, 40 %). ^{1}HNMR (400 MHz, $CDCl_3$) δ: 8.17 (s, 2H), 7.59 (d, J=8.2, 4H), 7.55 (s, 2H), 7.43 (d, J=8.2, 4H), 2.45 (s, 6H). ^{13}CNMR (100 MHz, $CDCl_3$) δ: 195.88, 140.66, 140.46, 136.90, 134.76, 131.51, 130.89, 126.53, 126.25, 119.27, 97.57, 87.31, 32.97. HRMS(ESI) calcd. for

$C_{30}H_{18}O_2S_4$ $[M+H]^+$: 539,02624, found: 539.02457.

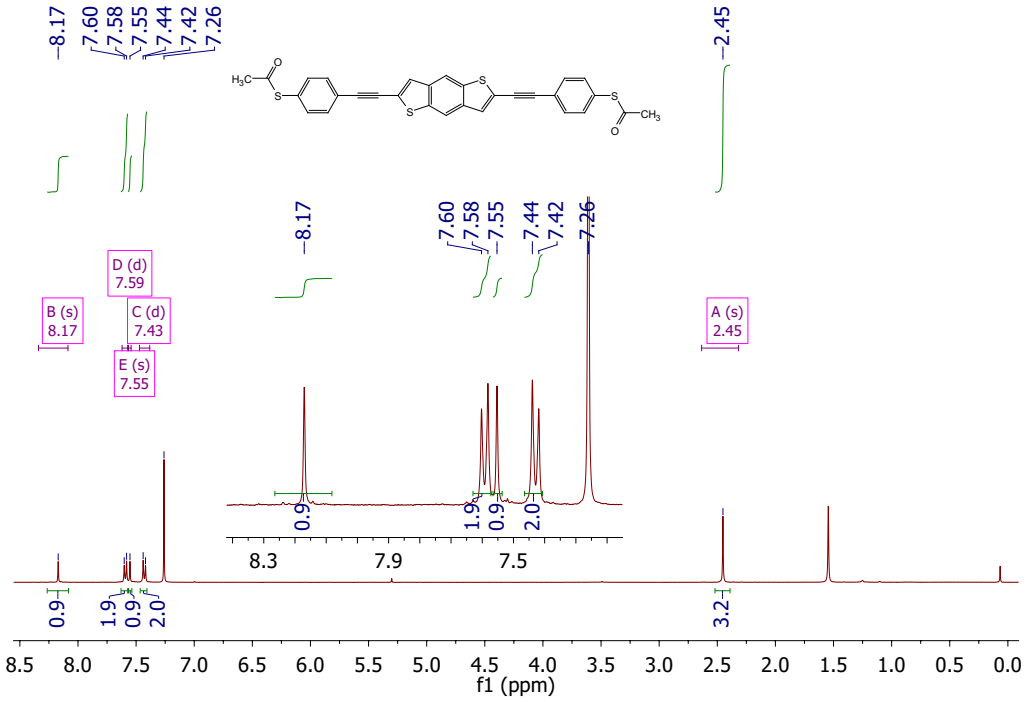

Figure S4: ^{1}HNMR spectrum of **BDT-1**

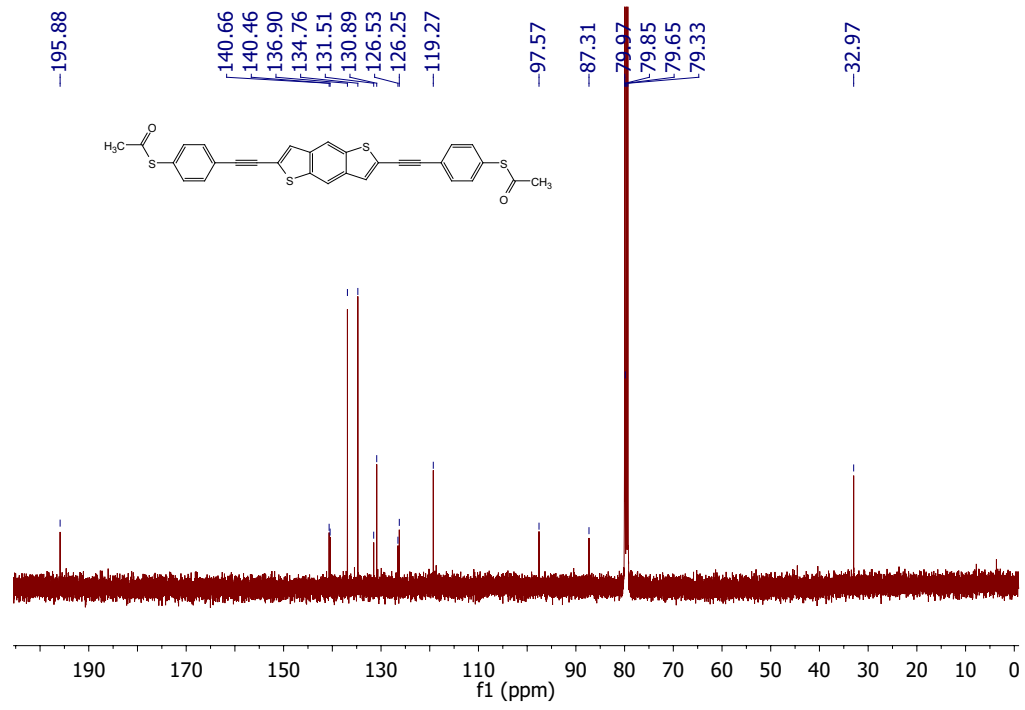

Figure S5: ^{13}CNMR spectrum of **BDT-1**

1.1.2 Synthesis of BDT-2

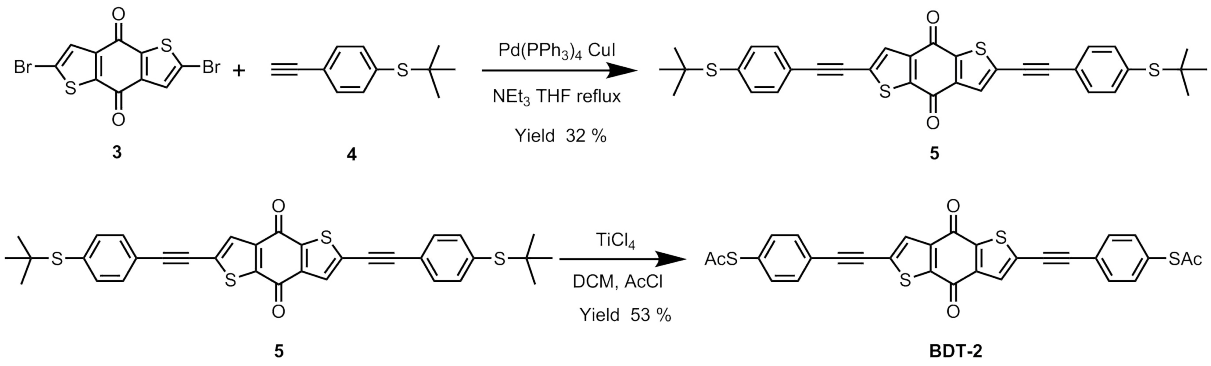

Figure S6: Synthetic route for **BDT-2**

2,6-Bis[(4-tert-butylthiophenyl)ethynyl]benzo[1,2-b:4,5-b']dithiophene-4,8-dione (5). 2,6-dibromobenzo[1,2-b:4,5-b']dithiophene-4,8-dione (**3**; 200 mg, 0.53 mmol) and 1-tert-butylthio-4-ethynylbenzene (**4**; 230 mg, 1.21 mmol) were dissolved in mixture of fresh distilled Et_3N (5 mL) and anhydrous THF (10 mL). After degassing, the catalysts $Pd(PPh_3)_4$ (30 mg, 0.03 mmol) and CuI (5 mg, 0.03 mmol) were added. The reaction mixture was refluxed for overnight under N_2. The crude solid was purified by column chromatography to give **5** (100 mg, 32 %). ^{1}HNMR (400 MHz, $CDCl_3$) δ: 7.71 (s, 2H), 7.55 (d, J=8.2, 4H), 7.50 (d, J=8.2, 4H), 1.31 (s, 18H). ^{13}CNMR (100 MHz, $CDCl_3$) δ: 173.33, 143.91, 142.55, 137.24, 135.17, 131.73, 131.56, 130.31, 121.70, 98.14, 82.55, 46.81, 31.02.

2,6-Bis[(4-acetylthiophenyl)ethynyl]benzo[1,2-b:4,5-b']dithiophene-4,8-dione (BDT-2).[S24] $TiCl_4$ (0.04 mL, 0.364 mmol) was added drop-wise to a solution of compound **5** (100 mg, 0.167 mmol) and $CH_3C(O)Cl$ (0.03 mL, 0.377 mmol) in CH_2Cl_2 at 0 °C. The resulting mixture was stirred at room temperature for 1 h and the conversion was monitored by TLC (hexanes/CH_2Cl_2, 2:1). Upon completion, the reaction was quenched with water (10 mL). The crude solid was purified by column chromatography to give **BDT-2** (50 mg, 53 %). ^{1}HNMR (400 MHz, $CDCl_3$) δ: 7.73 (s, 2H), 7.59 (d, J=8.2, 4H), 7.45 (d, J=8.2, 4H), 2.46 (s, 6H). ^{13}CNMR (100 MHz, $CDCl_3$) δ: 195.59, 175.96, 145.20, 136.95, 134.87, 134.20, 133.15, 132.57, 132.50, 125.24, 100.42, 85.49, 33.01. HRMS(ESI) calcd. for $C_{30}H_{17}O_4S_4$ $[M+H]^+$:

569,00042, found: 568.99887.

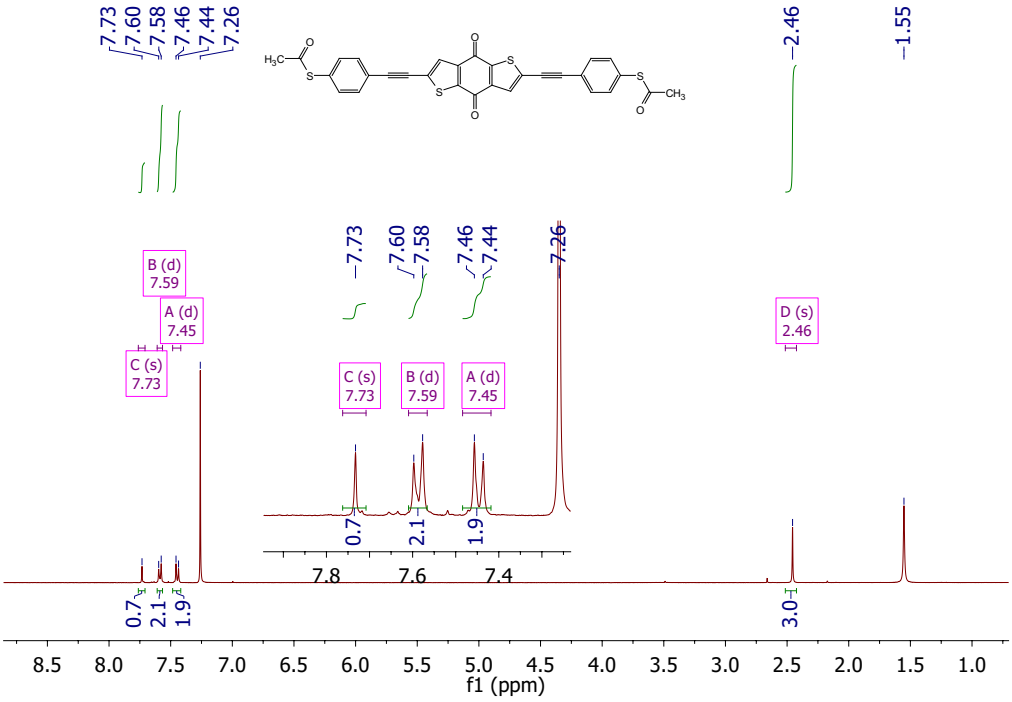

Figure S7: ^{1}HNMR spectrum of **BDT-2**

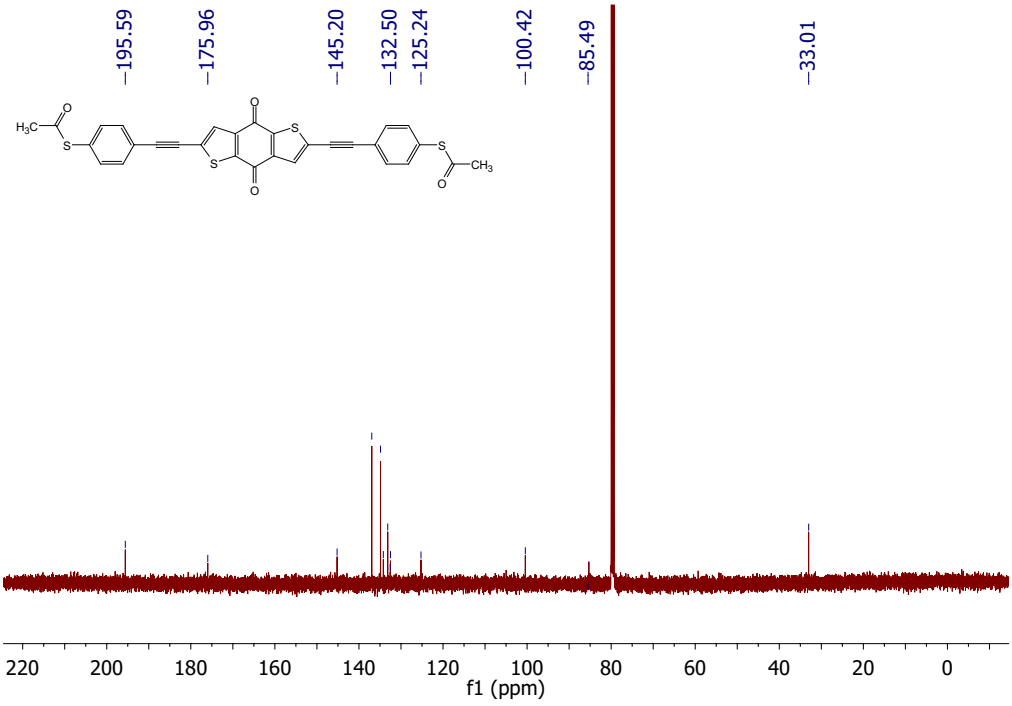

Figure S8: ^{13}CNMR spectrum of **BDT-2**

1.1.3 Synthesis of BDT-3

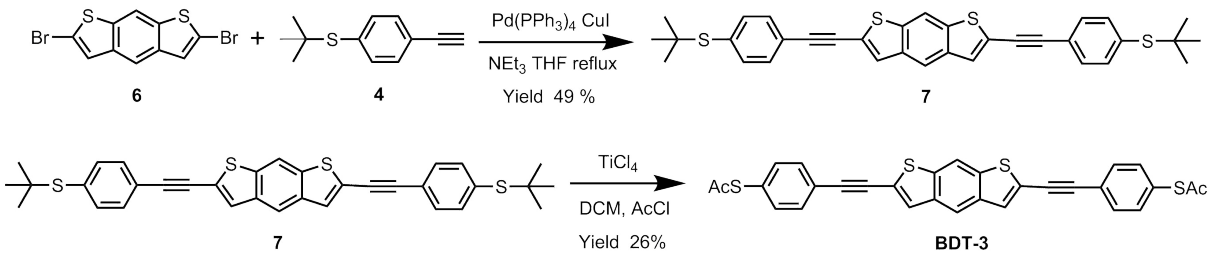

Figure S9: Synthetic route for **BDT-3**

2,6-Bis[(4-tert-butylthiophenyl)ethynyl]benzo[1,2-b:5,4-b']dithiophene (7). 2,6-dibromobenzo[1,2-b:5,4-b']dithiophene (**6**; 50 mg, 0.143 mmol) and 1-tert-butylthio-4-ethynylbenzene (**4**; 68 mg, 0.358 mmol) were dissolved in mixture of fresh distilled Et_3N (5 mL) and anhydrous THF (10 mL). After degassing, the catalysts $Pd(PPh_3)_4$ (16 mg, 0.014 mmol) and CuI (2.7 mg, 0.014 mmol) were added. The reaction mixture was refluxed overnight under N_2. The crude solid was purified by column chromatography to give **7** (40 mg, 49 %). ^{1}HNMR (400 MHz, $CDCl_3$) δ: 8.16 (s, 1H), 8.14 (s, 1H), 7.56 (s, 2H), 7.54 (d, J=4, 4H), 7.51 (d, J=4, 4H), 1.31 (s, 18H). ^{13}CNMR (100 MHz, $CDCl_3$) δ: 141.35, 140.05, 139.89, 136.77, 134.10, 131.29, 125.64, 125.38, 120.85, 117.39, 97.51, 86.99, 49.30, 33.67.

2,6-Bis[(4-acetylthiophenyl)ethynyl]benzo[1,2-b:5,4-b'] dithiophene (BDT-3).[S24] $TiCl_4$ (0.042 mL, 0.388 mmol) was added drop-wise to a solution of compound **(7)** (100 mg, 0.176 mmol) and $CH_3C(O)Cl$ (0.03 mL, 0.397 mmol) in CH_2Cl_2 at 0 °C. The resulting mixture was stirred at room temperature for 10 min and the conversion was monitored by TLC (hexanes/CH_2Cl_2 2:1). Upon completion the reaction was quenched with water (10 mL). The crude solid was purified by column chromatography to give **BDT-3** (25 mg, 26 %). ^{1}HNMR (400 MHz, $CDCl_3$) δ: 8.17 (s, 1H), 8.15 (s, 1H), 7.59 (d, J=7.2, 4H), 7.58 (s, 2H), 7.43 (d, J=8.2, 4H), 2.45 (s, 3H). ^{13}CNMR (100 MHz, $CDCl_3$) δ: 195.88, 141.43, 140.03, 136.90, 134.76, 131.51, 131.48, 126.27, 126.50, 120.94, 117.42, 97.22, 87.15, 32.97. HRMS(ESI) calcd. for C30H18O2S4 $[M+H]^+$: 539,02624, found: 539.02476.

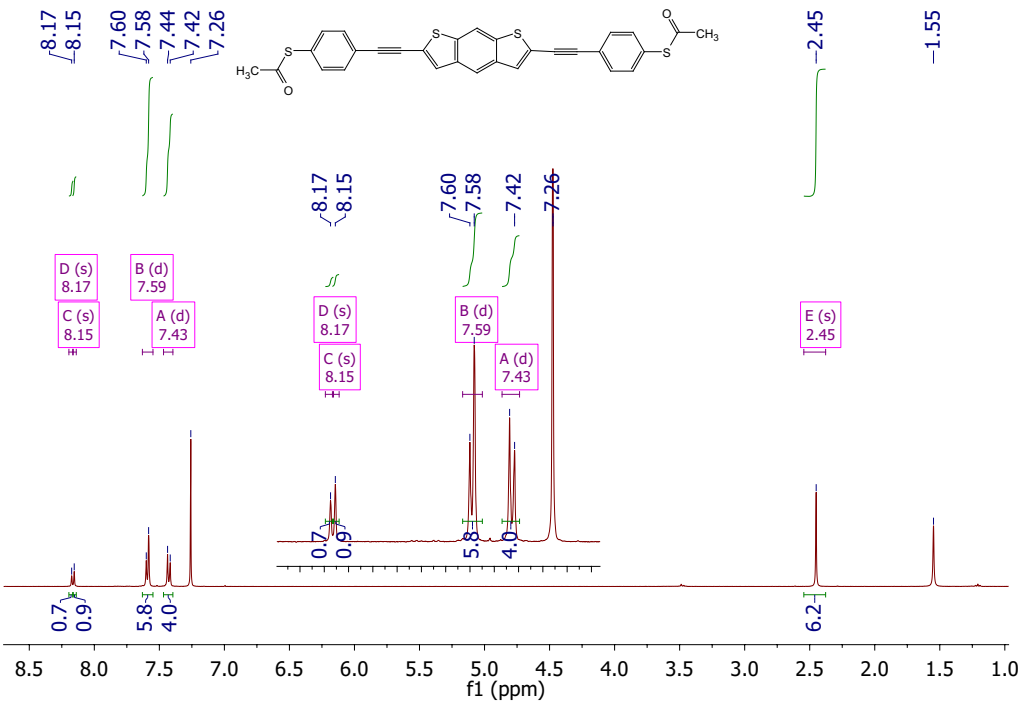

Figure S10: ^{1}HNMR spectrum of **BDT-**3

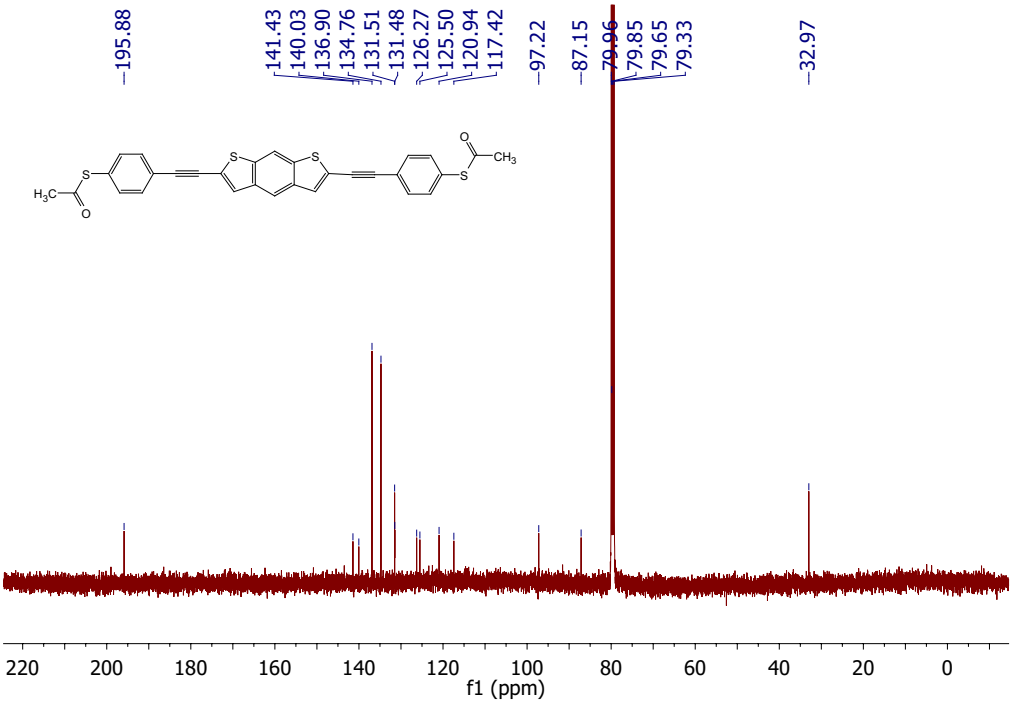

Figure S11: ^{13}CNMR spectrum of **BDT-**3

1.2 Self-assembled Monolayers

The SAMs of **BDT-*n*** were formed via *in situ* deprotection[S6,S25] on template-stripped Au substrates.[S26] Freshly template-stripped substrates were immersed into 3 mL of 50 µM solutions of the thioacetate precursors in freshly distilled toluene inside a nitrogen-filled glovebox and sealed under a nitrogen atmosphere. The sealed vessels were kept inside a nitrogen flow box[S27] (O_2 below 3 %, RH below 15 %) overnight; all subsequent handling and EGaIn measurements were performed inside the flowbox. 1.5 h prior to measurement, 0.05 mL of 17 mM diazabicycloundec-7-ene(DBU) in toluene was added to the precursor/substrate solution. The substrates were then rinsed with toluene and allowed to dry for 30 min before performing the measurements. The SAM of **AQ** was prepared according to the reported methods[S1] in dichloromethane (DCM).

1.3 Characterization

The SAMs of **BDT-*n*** were characterized by XPS (laboratory and synchrotron), NEXAFS, UPS and water contact angles. In some cases, SAMs of $CH_3(CH_2)_{15}SH$ or $CH_3(CH_2)_{17}SH$ on Au were used as a reference.

1.3.1 UV-Vis

UV-Vis measurements were carried out on a Jasco V-630 spectrometer, in 1 cm fused quartz cuvettes with concentrations of 10^{-5} mol/L in toluene. The calculated optical band gaps are summarized in Table S2.

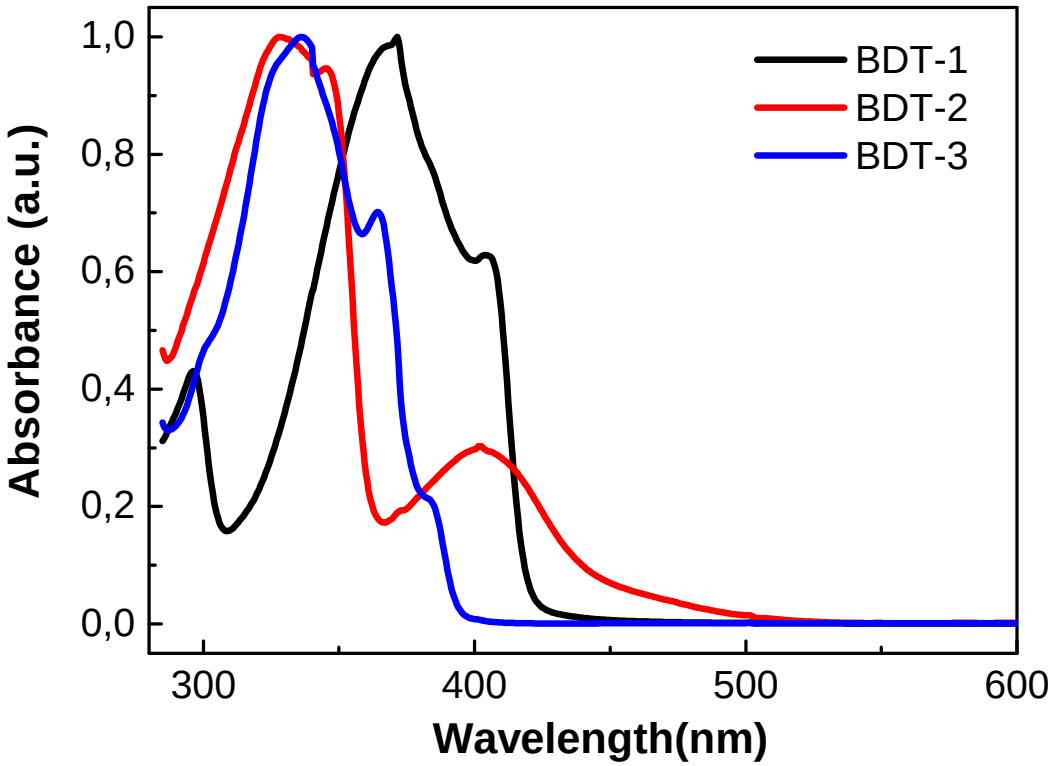

Figure S12: Normalized UV-Vis absorption spectra for **BDT-1**(black), **BDT-2**(red), **BDT-3**(blue).

1.3.2 Water Contact Angles

Contact Angles were measured under ambient conditions on a SCA20 Dataphysics instrument. Contact angles were obtained by applying 3 µL water droplets on SAMs modified Au substrates using the sessile drop method. The contact angles were measured at two different samples for each molecule, three different locations on each sample and the results were averaged with the standard deviation as the error.

1.3.3 Ultraviolet Photoelectron Spectroscopy

UPS measurements were performed using a VG microtech clam 100 spectrometer and an ultraviolet (He I, 21.2 eV) light source. Samples of SAMs were prepared as described in the Experimental and quickly transferred into the entry lock of the vacuum system. The base pressure of the measurement chamber was $<5 \times 10^{-9}$ mbar. A bias of -4 V was applied to

the sample holder to obtain the secondary electron cut-off (SEC). HOPS onsets were found by fitting multiple Gaussian functions

$$He^{-\frac{(x-\mu)^2}{2\sigma^2}}$$

to the spectra, on top of the linear slope of the Fermi edge. The onset for the HOPS is found at $\mu + 2\sigma$ for the peak at the highest kinetic energy. The vacuum levels for the two samples are found by adding the photon energy, 21.2 eV, to the SEC. The binding energy scale is in reference to these vacuum levels.

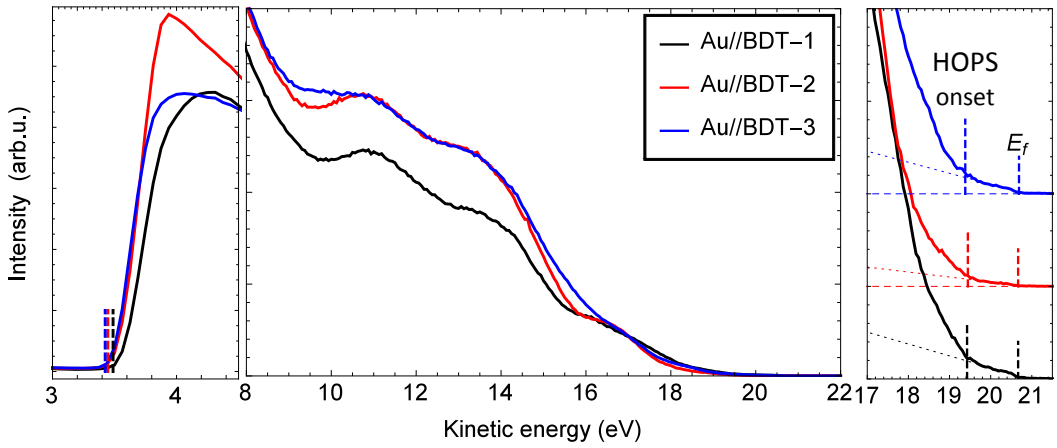

Figure S13: UPS spectra for **BDT-1**(black), **BDT-2**(red), **BDT-3**(blue).

Table S2: Tabulated energy level data from calculations (DFT) and experiments (CV, UPS, UV-Vis).

	CV		**UPS**		**DFT (gas-phase)**		**UV-Vis**
	HOMO	**LUMO**	**HOPS**[a]	$\mathbf{E_f}$	**HOMO**	**LUMO**	$\mathbf{E_g}$
BDT-1	-	-	-5.4	-4.2	-5.38	-2.33	2.95
BDT-2		-3.79	-5.4	-4.2	-5.95	-3.56	2.79
BDT-3	-	-	-5.6	-4.1	-5.59	-2.12	3.15
AQ	-	-3.56[S23]	-6.1[S25]	-4.5[S25]	-5.98(-5.42[S28])	-3.24(-3.84[S28])	2.88[S28]

[a] HOPS (from UPS) is the onset of HOPS feature, corrected for instrument resolution.

1.3.4 XPS and NEXAFS

NEXAFS The **BDT-*n*** SAMs were characterized by X-ray photoelectron spectroscopy (XPS) and angle-resolved near-edge X-ray absorption fine structure (NEXAFS) spectroscopy. The measurements were performed at the HE-SGM beamline (bending magnet) of the synchrotron storage ring BESSY II in Berlin, Germany using a custom-made experimental station equipped with a SCIENTA SES200 electron energy analyzer and a partial electron yield (PEY) detector.[S29]

The spectra acquisition in XPS was carried out in normal emission geometry with an energy resolution of $\sim 0.3\,\mathrm{eV}$ at an excitation energy of 350 eV and somewhat lower resolution at higher excitation energies. The binding energy (BE) scale of the XPS spectra was referenced to the Au $4f7/2$ emission at 84.0 eV.[S30] The spectra were fitted by symmetric Voigt functions and a Shirley-type background. To fit the S $2p_{3/2,1/2}$ doublets we used two peaks with the same full width at half-maximum (fwhm), a standard[S30] spin-orbit splitting of $\sim 1.2\,\mathrm{eV}$ (verified by fit), and a branching ratio of 2 (S$2p_{3/2}$/S$2p_{1/2}$). The fits were performed self-consistently: the same fit parameters were used for identical spectral regions.

The intensity values derived within the fitting procedure were used to calculate the effective thicknesses of the **BDT-*n*** SAMs. They were estimated on the basis of the C$1s$/Au $4f$ intensity ratio,[S31] assuming a standard exponential attenuation of the photoelectron signal[S32] and using the attenuation lengths typical of densely packed SAMs.[S33] The spectrometer specific constants were determined using the $CH_3(CH_2)_{17}S$ (C18) monolayer of well-defined thicknesses as a reference. In addition, molecular packing densities in the **BDT-*n*** SAMs were calculated, based on the S $2p$/Au $4f$ intensity ratio, relying on the established procedure[S34] using the same assumptions as in the case of the C$1s$/Au $4f$ evaluation. Only the part of the S $2p$ signal related to the thiolate was used. The C18 monolayer served as a reference; it has a molecular density of 4.63×10^{14} cm^{-2}, which corresponds a molecular footprint of 21.6 Å^2.[S35] The NEXAFS spectra were acquired at the C K-edge in the PEY acquisition mode with a retarding voltage of $-150\,\mathrm{V}$. Linear-polarized synchrotron light with

a polarization factor of 91 % was used. The energy resolution was ~ 0.3 eV. The incidence angle of the primary X-ray beam was varied from 90° (**E** vector in surface plane) to 20° (**E** vector nearly parallel to surface normal) in few steps to monitor the orientational order in the SAMs. This approach is based on the dependence of the cross-section of the resonant photoexcitation process on the orientation of the electric field vector of the synchrotron light with respect to the molecular orbital of interest (so-called linear dichroism in X-ray absorption).[S36] Raw NEXAFS spectra were normalized to the incident photon flux by dividing a spectrum of a clean, freshly sputtered gold sample and were reduced to the standard form by subtracting linear pre-edge background and normalizing to the unity edge jump (determined by a nearly horizontal plateau 40 eV to 50 eV above the respective absorption edges). The photon energy scale was referenced to the most intense $\pi*$ resonance of highly oriented pyrolytic graphite at 285.38 eV.[S37]

The C 1*s* and S 2*p* XPS spectra of the **BDT-***n* SAMs are presented in Figure SI S14, along with the spectra for SAMs of $CH_3(CH_2)_{17}S$ (C18) for reference. The C1*s* spectra of the **BDT-***n* SAMs exhibit a strong peak at 284.7 eV to 285.0 eV assigned to the molecular backbone. The binding energy of this peak is higher for **BDT-**2 monolayer (285.0 eV) as compared to the **BDT-**1 and **BDT-**2 SAMs (284.7 eV to 284.8 eV), which can be explained by the effect of the oxygen atoms in the quinone core of **BDT-**2. For all **BDT-***n* SAMs, the peak is noticeably broader than that for C18/Au, since it contains contributions of several different functional groups such as oligophenylenes,[S38–S40] phenyl,[S41,S42] and thiophene.[S43] In addition, there are much weaker signals at higher binding energies, which can be partly associated with the thiophene moieties[S43] and partly stem from contamination (which could not be avoided completely). The S 2p XPS spectra of the **BDT-***n* SAMs exhibited characteristic signals of thiolate (**1**)[S42] at 162.0 eV (S $2p_{3/2}$) and a joint signal of the thiophene moieties (**2**) and unbound SAc groups (**3**) at higher binding energies. For the **BDT-**1 and **BDT-**3 SAMs the positions of the latter signals are very close, in agreement with literature reports,[S43,S44] merging to a joint doublets at 163.8 eV to 163.9 eV (S $2p_{3/2}$). For the **BDT-**2 SAMs, the

position of the thiophene-related doublet (**3**) is shifted to 164.5 eV (S $2p_{3/2}$) due to the effect of the oxygen atoms in the quinone group.

For all **BDT-***n* SAMs, the intensity of the joint thiophene-thioacetate feature is much higher than that of the thiolate groups, which can only be explained by the differences in the attenuation, typical for an upright orientation of thiol-terminated molecules[S44] and molecules with sulfur-containing groups in the molecular backbone.[S45] This observation suggests that the molecules in the **BDT-***n* SAMs are assembled upright, in the expected SAMs fashion, with one of the terminal (deprotected) thioacetate groups bound to the substrate and the another (partially deprotected) one exposed to the SAMs-ambient interface,[S25] where it can be contacted by the top electrodes. Also of interest is the fact that the intensities of the thioacetate- and thiophene-related doublets in the S $2p$ spectrum of the **BDT-**2 SAMs are almost equal, in spite of two S atoms in the thiophene-based core as compared to only one in the thioacetate group, which can only be explained by the attenuation effects, once more suggesting upright molecular orientation.

We computed the packing densities and effective thicknesses based on the intensities of the XPS peaks and doublets. The effective thickness values correlate coarsely between synchrotron- and laboratory-XPS experiments; these results are compiled in Table 1. In agreement with the S $2p$ data, the derived values of the effective thickness suggest upright molecular orientation in all **BDT-***n* SAMs, even though with a certain tilt. These results are summarized in Table 1.

The NEXAFS spectra of the **BDT-***n* SAMs are presented in Fig. S15. The 55° spectra, characteristic of the electronic structure only,[S36] exhibit a superposition of the characteristic absorption resonances of the OPE compounds[S40] and thiophene moieties. The dominant, slightly asymmetric π^* resonance at $\sim$ 285.0 eV is dominated by the $\pi_1{}^*$ resonance of OPE (at 285.0 eV as well)[S40] with a minor contribution from the $\pi_1{}^*$ resonance of thiophene at 285.6 eV.[S43] Another prominent π^*-like resonance resonance at 288.5 eV stems presumably from the $\pi_2{}^*$ resonance of OPE (at 285.6 eV).[S40] Further resonances in the edge region

are presumably related to the conjugated orbitals; the resonances at higher binding energies stems from the σ^*-orbitals, with contributions from all functional groups within the molecular backbones. No traces of contamination, above all a very pronounced resonance of carboxyl (most frequent contamination) at 288.8 eV,[S46] are observed, revealing that its portion is relatively low (in agreement with the XPS data).

The difference of the NEXAFS spectra acquired at the normal (90°) and the grazing (20°) incidence represent a fingerprint of molecular orientation in terms of linear dichroism in X-ray absorption. The difference spectra of the **BDT-***n* SAMs exhibit very small linear dichroism, as demonstrated by the 90° to 20° spectrum of the **BDT-**1 monolayer shown in Fig. S15, representative of the entire series. The most likely interpretation of this observation is that the average tilt angle of the molecules in the **BDT-***n* SAMs is close to 35°, corresponding to a magic tilt angle (55°) for the most relevant π^*-like orbitals. Considering that the difference spectra for the **BDT-**2 and **BDT-**3 SAMs exhibit small positive and negative peak, respectively, at the position of the dominant π^* resonance, one can assume a smaller molecular inclination ($\sim$ 30°) for the **BDT-**2 monolayer and a larger ($\sim$ 40°) - for the **BDT-**3 monolayer, which correlate with the effective thicknesses of these SAMs (Table 2).

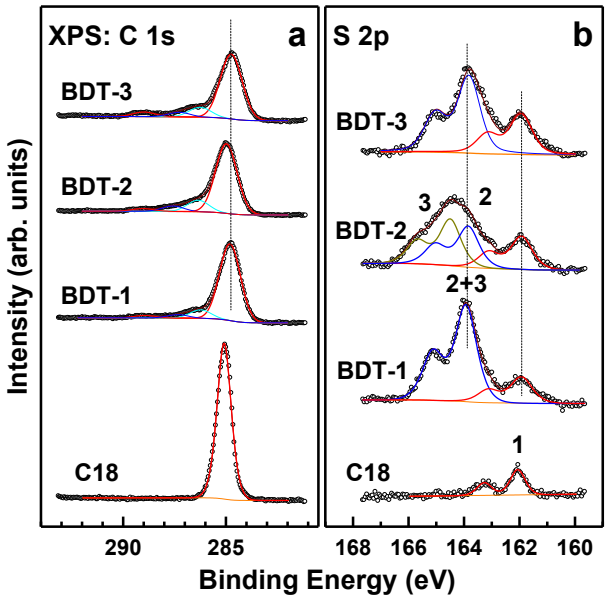

Figure S14: C 1s (a) and S 2p (b) synchrotron XPS spectra of the SAMs of **BDT-**n and C18 for reference. The spectra were acquired at a photon energy of 350 eV. The spectra are decomposed in the component peaks (C 1s) and doublets (S 2p); (see text for details).

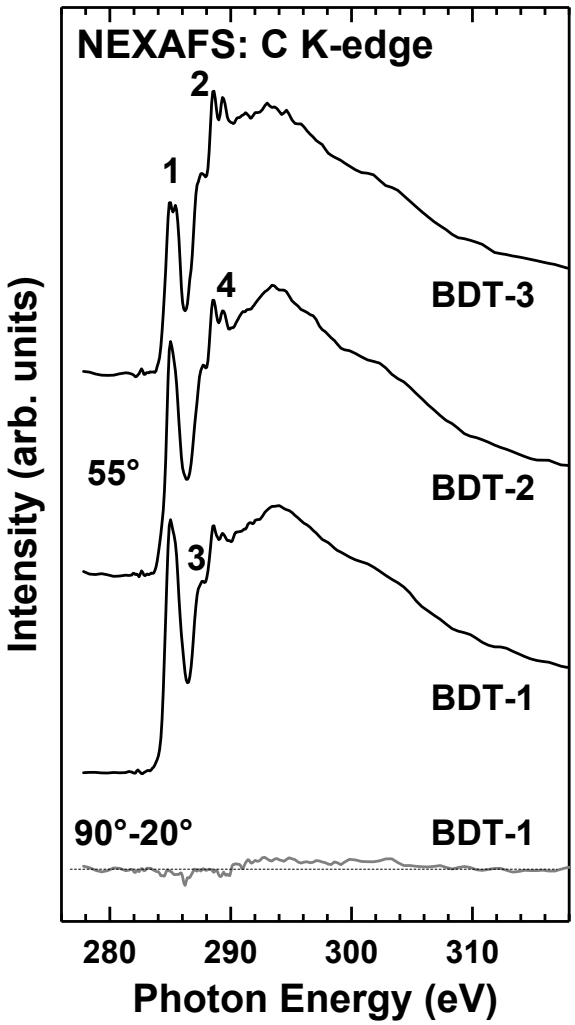

Figure S15: C K-edge NEXAFS spectra of the BDT SAMs. The 55° spectra are exclusively representative of the electronic structure of the monolayers.[S36] The 90° to 20° spectra, given on the **BDT-**1 SAM only, representative of the entire series, are representative of the molecular orientation.

There is also a general correlation between the XPS and NEXAFS data (Figure S15). The C K-edge NEXAFS spectra of all **BDT-***n* SAMs are quite similar, exhibiting absorption structure that can be associated with the individual functional groups of these molecules, with the dominance of the OPE-stemming resonances. We found negligible (**BDT-**1) or quite small (**BDT-**2 and **BDT-**3) linear dichroism. Taken together with all other data and analysis of the dichroism data, this result suggests that the tilt angle of the molecules in these SAMs is close to 35°, with a slightly smaller and larger molecular inclination for the

SAMs of **BDT-**2 and **BDT-**3, respectively, which correlates to the effective thicknesses.

1.3.5 Cyclic Voltammetry

Cyclic voltammetry (CV) was carried out with a Autolab PGSTAT100 potentiostat in a three-electrode configuration where the working electrode was platinum electrode, the counter electrode was a platinum wire, and the pseudo-reference was an Ag wire that was calibrated against ferrocene (Fc/Fc^+). **BDT-**2 with the concentration of 0.001 M in ODCB-CH_3CN (9:1) solution containing Bu_4NPF_6 (0.1 M) was scanned at a rate of 100 mV/s. The first half-wave reduction potential appears at -1.01 V and second one appears at -1.51 V. The LUMO of **BDT-**2 is determined from the first half-wave reduction potential, with E_{HOMO} of ferrocene at -4.8 eV (LUMO = -($E_{1/2}^{red1}$ + 4.8) eV).

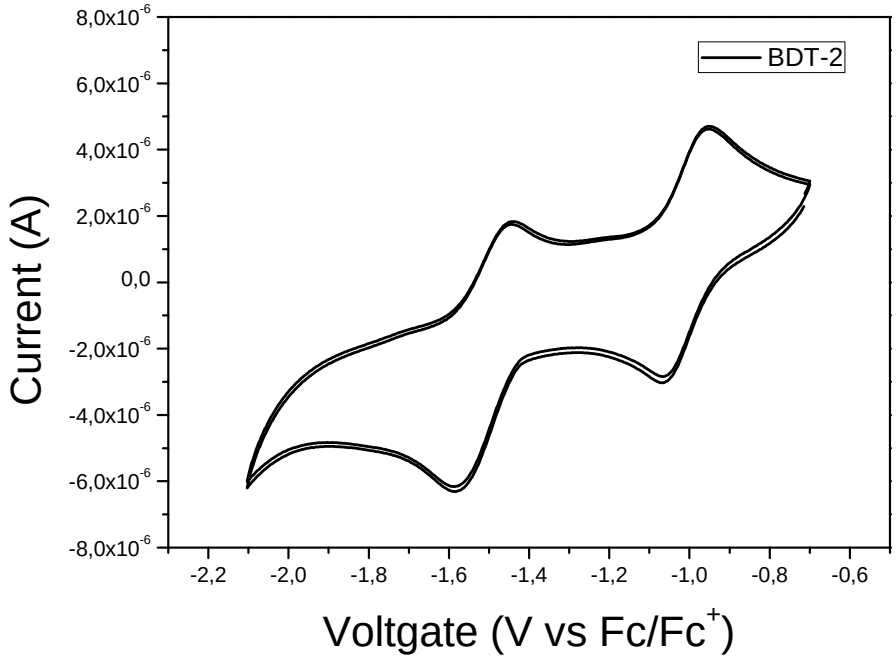

Figure S16: Cyclic voltammetry of **BDT-**2 with a scan rate of 100mV/s.

2 Electrical Measurements

2.1 EGaIn

The details of the EGaIn setup are described elsewhere.[S1,S6] Briefly, EGaIn measurements were carried in the nitrogen flowbox. For each SAM, at least 10 junctions were measured on each of three different substrates by applying a bias from $0.00\,\mathrm{V} \rightarrow 1.00\,\mathrm{V} \rightarrow -1.00\,\mathrm{V} \rightarrow 0.00\,\mathrm{V}$ with steps of $0.05\,\mathrm{V}$. At least 20 trace/re-trace cycles were measured for each junction; only junctions that did not short over all 20 cycles were counted as "working junction" for computing yields. A new EGaIn tip was prepared every 4 junctions.

J-V Data Processing: Data was acquired as described above and then parsed in a "hands-off" manner using Scientific Python to produce histograms of J for each value of V and the associated Gaussian fits (using a least-squares fitting routine). The confidence intervals for μ_{logJ} (Gaussian mean) depicted as error bars in the J/V plots were calculated using $\alpha = 0.95$ from σ_{logJ} (standard deviation) taken from Gaussian fits and a number of degree of freedom equal to the $N_{\mathrm{junctions}} - 1$. The value of t chosen for **BDT-**1 and **BDT-**3 is 2.04 (degree of freedom is 31) and **BDT-**2 is 2.05 (degree of freedom is 29).

Differential Conductance Heatmap: The J-V plots were smoothed by the polynomial model and the derivative of the current density (J) relative to the voltage (dJ/dV) were computed individually from each J-V plot. Then we constructed a 2D histogram of these dJ/dV values by logarithmically binning them for each bias voltage and plotting them, resulting in a heatmap with on the x-axis the bias voltage, on the y-axis the log (dJ/dV) and on the z-axis (in colour scale) the number of counts.

Table S3: Summary of Transition Voltage of **BDT-**1, **BDT-**2, **BDT-**3 and **AQ** obtained from EGaIn measurements

	BDT-1	**BDT-2**	**BDT-3**	**AQ**
$V_{\mathrm{trans}+}$	0.652 ± 0.002	0.209 ± 0.068	0.597 ± 0.042	0.257 ± 0.010
$V_{\mathrm{trans}-}$	-0.776 ± 0.054	-0.200 ± 0.059	-0.689 ± 0.068	-0.299 ± 0.099

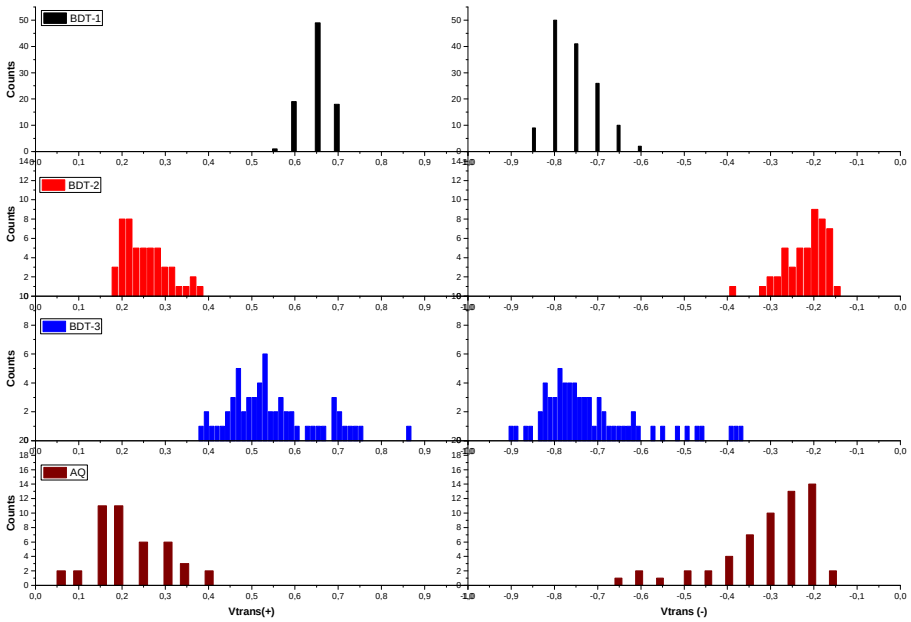

Figure S17: Transition Voltage Histogram of junctions comprising Au/**BDT-**1, 2, 3 and **AQ**//EGaIn. (**BDT-**1:Black, **BDT-**2:Red, **BDT-**3:Blue and **AQ**: Dark red.)

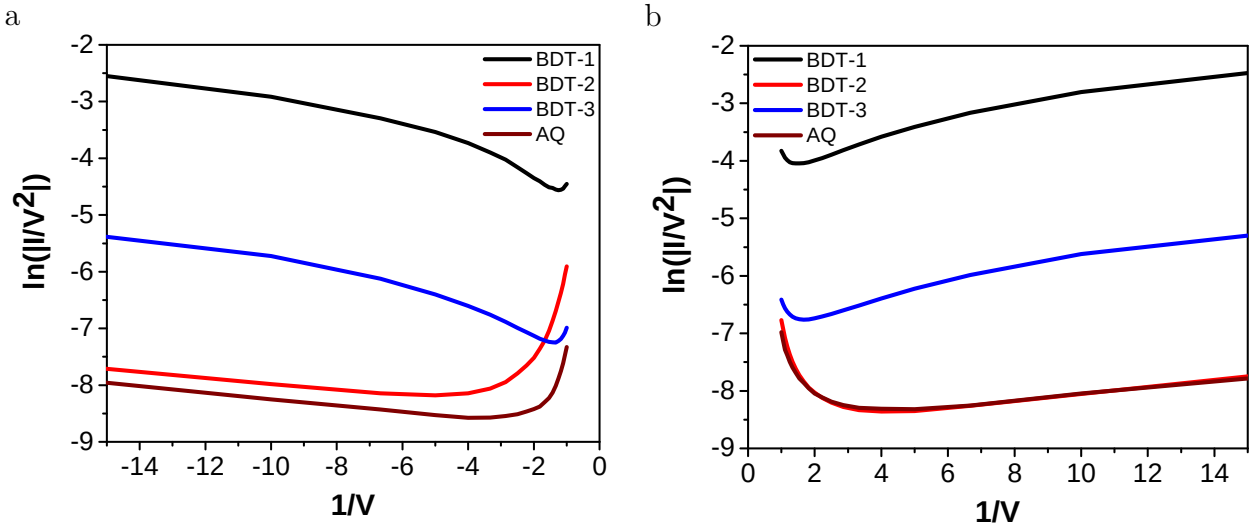

Figure S18: Transition voltage spectroscopy of Au/SAM//EGaIn junctions from Gaussian fitted J-V curves obtained by EGaIn: a) negative bias b) positive bias.

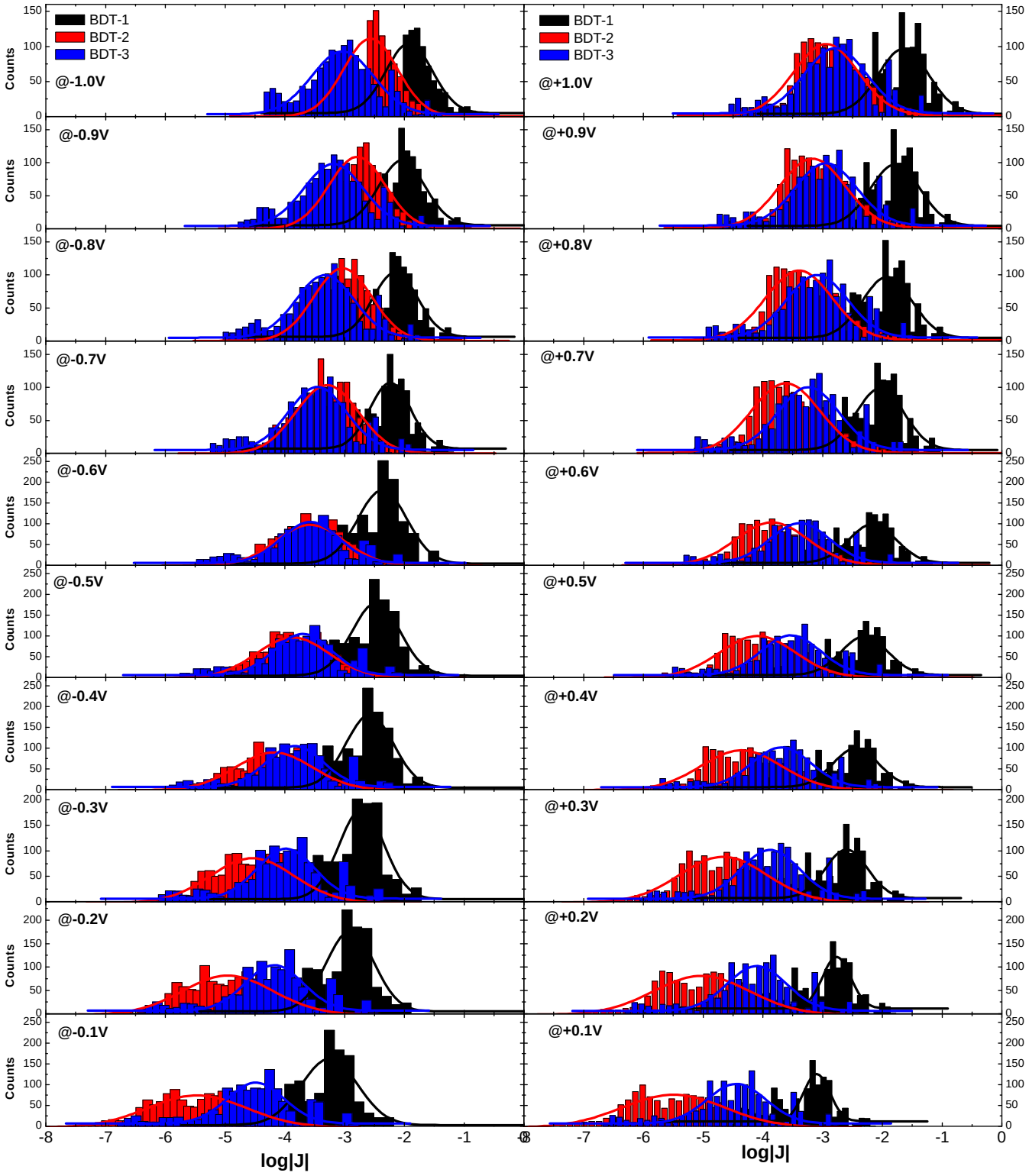

Figure S19: log $|J(\mathrm{Acm}^{-2})|$ Histogram of junctions comprising $\mathrm{Au}^{\mathrm{TS}}$/**BDT-**1, 2, 3//EGaIn at at different bias: Left panel top to bottom starting from -1.0 V to -0.1 V and right panel top to bottom starting +1.0 V to +0.1 V.

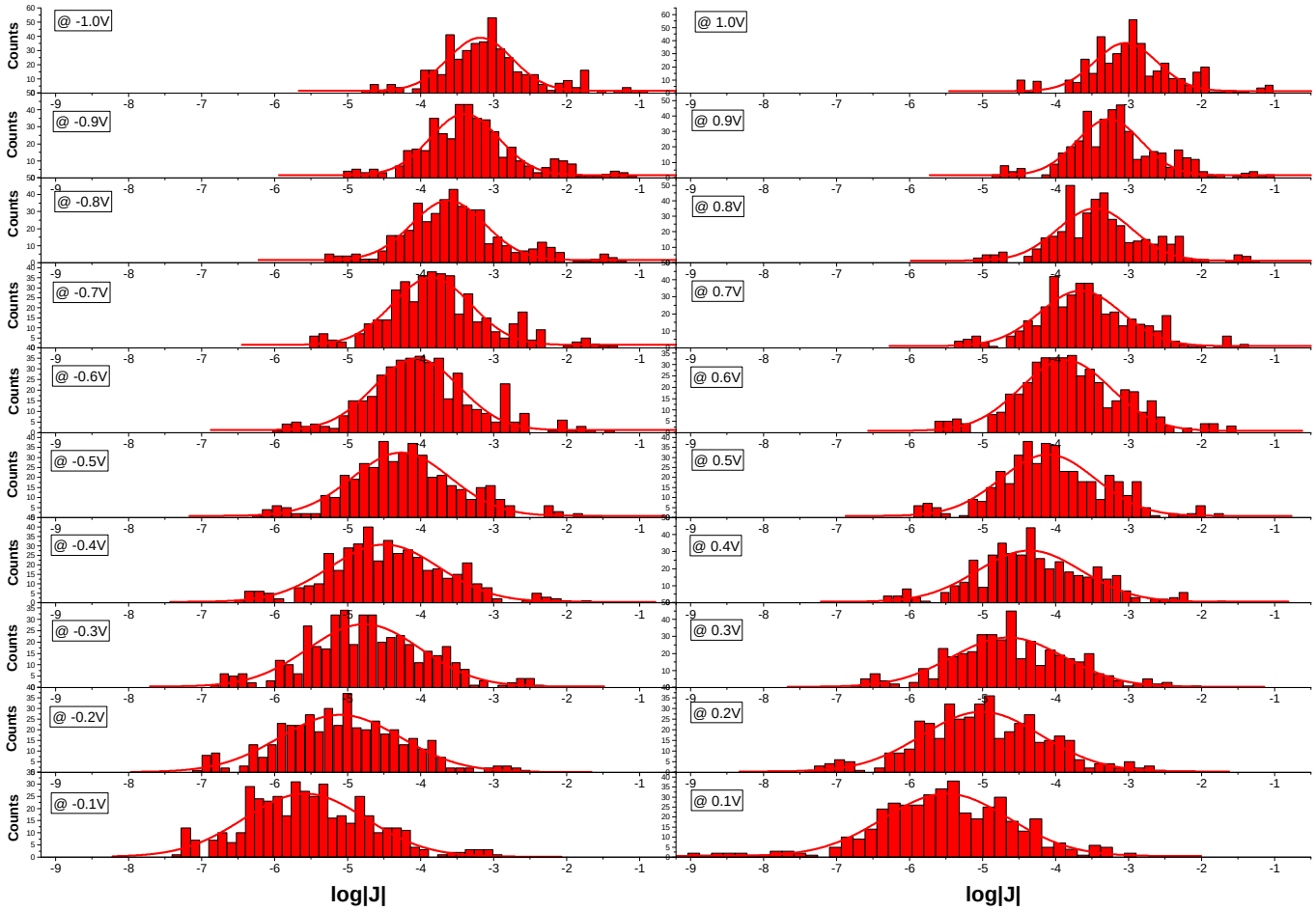

Figure S20: log $|J(\mathrm{Acm}^{-2})|$ Histogram of junctions comprising Au-on-mica/**AQ**//EGaIn at at different bias: Left panel top to bottom starting from -1.0 V to -0.1 V and right panel top to bottom starting +1.0 V to +0.1 V.

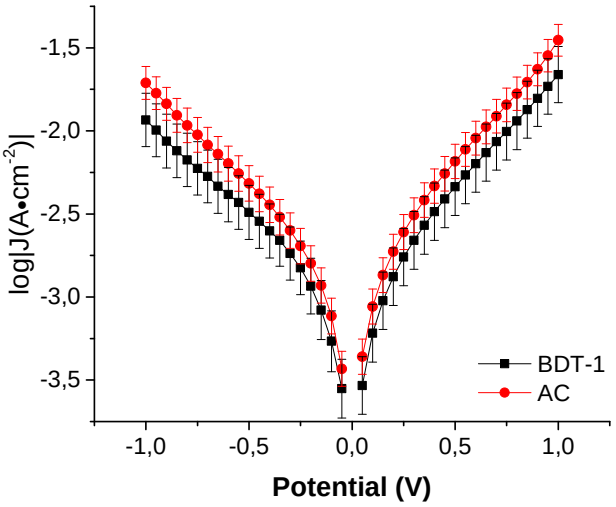

Figure S21: log plots of $|J(\mathrm{Acm}^{-2})|$ vs. V of $\mathrm{Au}^{\mathrm{TS}}$/SAM//EGaIn junctions of **BDT-1** (black) and **AC**(red) (reported somewhere else[S6]). Each data point is the peak of a Gaussian fit of $\log|J|$ for that voltage and error bars are 95% confidence intervals.

The asymmetry of J/V plots: We calculated R by dividing each value of J at positive bias into the corresponding value at negative bias for each value of $|V|$ and then fitting a Gaussian to the resulting histogram of $\log|R|$ and expressing the error as the standard deviation of the fit (see Fig. S22). In EGaIn junctions, we usually do not consider junctions with $\log|R|$ below ± 1 as exhibiting rectifying behavior. Instead, we refer to it just as asymmetry. The direction of asymmetry of **BDT-**2 is different from the other three molecules above 0.2 V. One well-known cause of asymmetry is molecular states moving closer to E_{F} at one sign of bias, which happens when the molecule is strongly asymmetrically coupled to two different electrodes. For the BDT-series, the LUMO of **BDT-**2 is lower in energy than for any other molecule. We hypothesize that the LUMO of **BDT-**2 is sufficiently close to E_{F} that it comes close to resonance around 0.2 V, causing an increase in current-density. Presumably we would observe a jump in asymmetry for the other molecules if we were able to scan past ± 1 V. In fact, **AQ** already shows signs of bending towards negative values of $\log|R|$ around 0.8 V in the plot below.

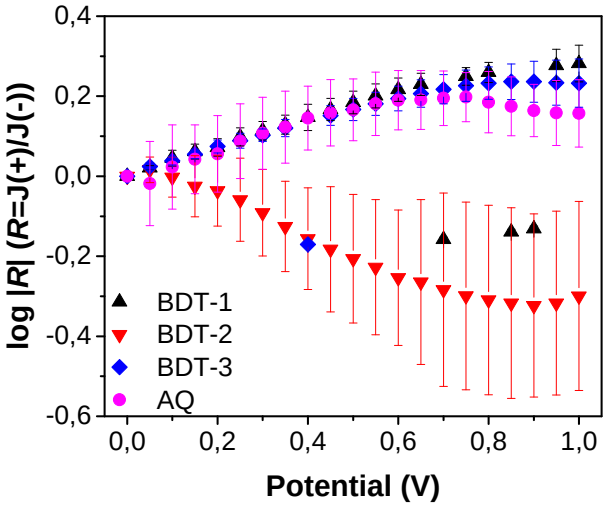

Figure S22: log|R| versus |V| plots of Au/SAM//EGaIn junctions comprising **BDT-**1, **BDT-**2, **BDT-**3 and **AQ**. The error bars are the standard deviation of the Gaussian fit.

2.2 CP-AFM

I-V measurements were performed on a Bruker AFM Multimode MMAFM-2 equipped with a Peak Force TUNA Application Module (Bruker.) The SAMs were contacted with a Au-coated silicon nitride tip with a nominal radius of 30 nm (NPG-10, Bruker, tip A: resonant frequency: 65 kHz, spring constant: 0.35 N/m; tip B: resonant frequency: 23 kHz, spring constant: 0.12 N/m; tip C: resonant frequency: 56 kHz, spring constant: 0.24 N/m; tip D: resonant frequency: 18 kHz, spring constant: 0.06 N/m. Tip A was chosen in this work) in TUNA mode. The AFM tip was grounded and the samples were biased from −1.0 V to +1.0 V and from +1.0 V to −1.0 V on Au^{Mica} to record the I-V curves. The samples of **BDT-**2 were bias from −1.8 V to +1.8 V, since the current of **BDT-**2 is on the magnitude of pA from −1.0 V to +1.0 V. We plotted **BDT-**2 from the region of −1.0 V to +1.0 V for easy comparison with **BDT-**1 and **BDT-**3. 11 trace/re-trace cycles per junction were performed and the top electrode was removed from SAMs between junctions. New tips were replaced between samples. The total number of I-V traces recorded by CP-AFM is summarized in Table S4.

Processing. All raw data were processed algorithmically using Scientific Python to generate

histograms, Gaussian fits, extract transition voltages and construct differential conductance heatmap plots.

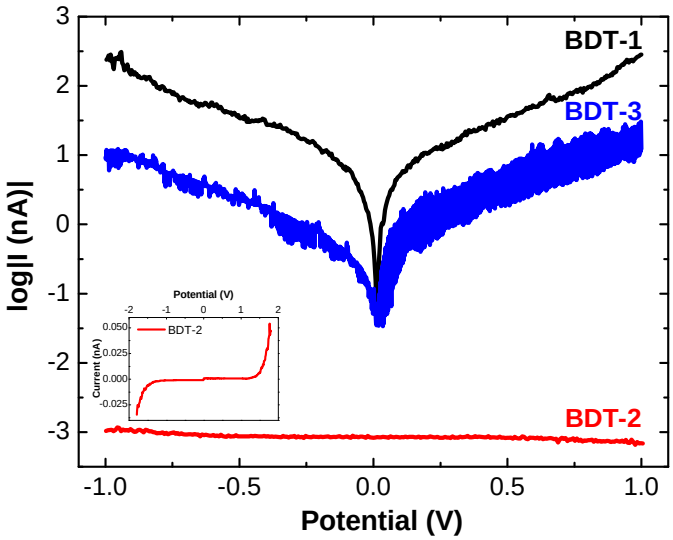

Figure S23: Plots of $\log|I(\text{nA})|$ versus V of Au-on-mica/SAM//Au^{AFM} junctions comprising SAMs of **BDT-**1 (black), **BDT-**2 (blue) and **BDT-**3 (red) without error bars. Each datum is the peak of a Gaussian fit of $\log|I|$ for that voltage. The inset shows the Gaussian fitted I/V trace for **BDT-**2 on linear scale to $\pm 1.8\,\text{V}$.

The difference in conductivity between **BDT-**1 and **BDT-**3 is nearly identical for both EGaIn and CP-AFM measurements across the entire bias window. The current of **BDT-**2 was below the detection limit of our CP-AFM setup in the low-bias regime, however, at $\pm 1\,\text{V}$, the difference between **BDT-**1 and **BDT-**2 is 10^5 larger for CP-AFM than for EGaIn.

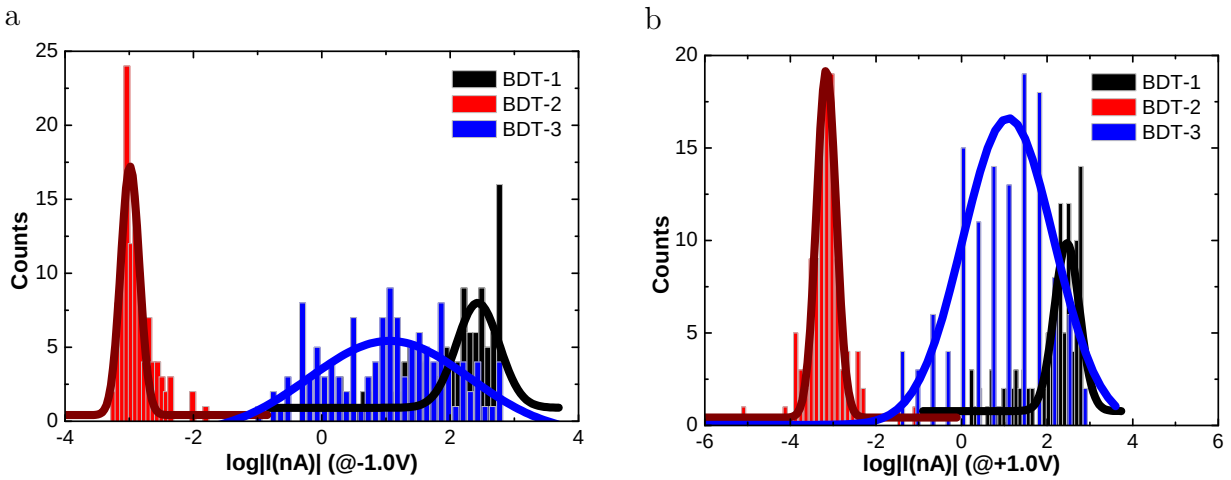

Figure S24: a) log $|I(\mathrm{nA})|$ Histogram of Au-on-mica/SAM//$\mathrm{Au}^{\mathrm{AFM}}$ junctions at -1.0 V. b) log $|I(\mathrm{nA})|$ Histogram of $\mathrm{Au}^{\mathrm{Mica}}$/SAM//$\mathrm{Au}^{\mathrm{AFM}}$ junctions at +1.0 V.

Table S4: Summary of I-V traces recorded by CP-AFM

SAMs	**Number of junctions**	**Number of traces**
BDT-1	10	110
BDT-2	10	110
BDT-3	12	136

3 Computational Methodology

We performed the calculations using the *Orca 4.0.0.1* software package[S47,S48] and the *Artaios-030417* software package.[S49,S50] The procedure is described below step-by-step.

3.1 Molecular Geometry Optimization

We optimized all the four molecules terminating with dithiols. We used ORCA DFT package and utilized the default Ahlrichs $def2-SVP$ basis sets (ORCA option *Acc-Opt*, that calls the BP functional).[S51] This optimized gas-phase geometry was then used for all the following steps.

3.2 Single Point Energy Calculations

3.2.1 Gas-Phase energies

We used the ORCA DFT package also for calculating the gas-phase energies for all the four molecules. We used the minimized geometries terminating with thiols to calculate the single-point gas-phase energies using $B3LYP/G\ LANL2DZ$. The HOMO-LUMO energies obtained from these gas-phase energy calculations are tabulated in Table S2.

3.2.2 Attaching Electrodes

We attached the minimized geometries to two 18-atom Au standard electrode clusters after manually deleting the terminal thiols' hydrogen atoms. The geometries of the electrode clusters used in these calculations consisted of 18 Au atoms per electrode, with two layers arranged in a hexagonal close-packed fcc Au-111 surface. The Au-Au distance was set to 2.88 Å, from the experimental lattice values of the bulk gold.[S52] This is all similar to previously reported work.[S53] S-Au distance was maintained at a value of 2.48 Å and S is attached to the center of the hexagonal close-pack hollow site, taken from literature.[S54] We kept these geometrical parameters of the electrodes and the electrode material same throughout all these calculations, so that qualitative comparisons could be drawn. This junction geometry of the molecule attached via the Sulphur linker to the two Au metal clusters as electrodes was used for the next step.

3.2.3 Single Point Energy Calculations with Electrodes

After attaching the cores of the four molecules to the electrodes, we then calculated the single-point energies using the standard SCF convergence criteria using the ORCA DFT package. $B3LYP/G$ hybrid functional was applied and $LANL2DZ$ basis set was used. The energy values of the frontier π-states of the junction, *i.e.*, the HOPS (Highest Occupied π-state) and the LUPS (Lowest Unoccupied π-state) are tabulated in Table S5. The HOPS

and LUPS were found by manually looking at the electron density of the different energy levels until we found the orbitals with electron density spanning through the molecule's π backbone. The HOMO energy values of the four molecular junctions, for which the electron density was localized on the Au atom clusters, are also tabulated in the Table S5. Finally, to calculate the energy differences $E_{\mathrm{F}}-\mathrm{E}_{\mathrm{HOPS}}$ or $\mathrm{E}_{\mathrm{LUPS}}-E_{\mathrm{F}}$ in Fig. 5 of the main text, E_{F} value of EGaIn was taken to be -4.3 eV, as explained further in the last section.[S55]

Table S5: HOPS and LUPS from DFT for the four molecules when in the Au/Molecule/Au model junction along with the HOMO energy values (E_{F}) of Au clusters in the junction.

	DFT		
	HOPS	LUPS	HOMO of Au clusters
BDT-1	-5.80	-2.86	-4.84
BDT-2	-6.35	-3.84	-4.88
BDT-3	-5.91	-2.41	-4.83
AQ	-6.35	-3.44	-4.93

3.3 Transport Properties

For computing the electron transmission probability plots as function of energy of electron, we first ran single point energy calculations on structures terminating with only sulfur atoms, *i.e.*, by manually deleting the hydrogen atoms from the dithiols. Same basis sets were used as described above for the single point energy calculation. The hamiltonian and overlap matrices were generated from the output of these energy calculations, which served as the input for the *Artaios-030417* software tool for generating the transmission curves.[S49,S50] Thus, we used the input geometry of these four molecules without the terminal hydrogen atoms, computing the transmission of only the gas-phase molecule without the electrode clusters.

The reason for using the molecular system without electrode clusters is that we are only interested in the transmission of the molecule. These calculations are not simulations of an assembled junction; their purpose is to give insight into how the electronic structure affects

transmission, not to predict level-alignment. While the level-alignment will certainly be affected by the presence of electrodes, to ensure that the presence and absence of electrodes do not alter the electronic structure of the molecules, we plotted the molecular orbitals of the **BDT-***n* series with and without electrodes in Figure S25 to show that orbital shape and symmetry is preserved. We plotted HOPS for **BDT-**1 and **BDT-**3 and LUPS for **BDT-**2, *i.e.*, the orbitals that dominate the contribution to the electron transmission. The use of electrode clusters in these junctions is to identify the position of Fermi level of EGaIn junctions is physically realistic. Thus, we use the E_{F} of $-4.3\,\mathrm{eV}$ for scaling the energy axis of the transmission curve in the Figure 3 of the main text. It is known that the literature value for workfunction of clean gold is about $-5.2\,\mathrm{eV}$ to $-5.3\,\mathrm{eV}$ but the assembly of alkanethiolates atop the gold surface reduces this value by $0.85\,\mathrm{eV}$ ($-4.32\,\mathrm{eV}$ to $-4.4\,\mathrm{eV}$);[S56] further, the assembly of conjugated molecules result in a shift of $0.98\,\mathrm{eV}$.[S57,S58] Finally, the E_{F} of EGaIn has been reported as $-4.3\,\mathrm{eV}$ in the literature[S55] Thus, we use the value of $-4.3\,\mathrm{eV}$ for E_{F} which is close to the cumulative E_{F} value for the junctions comprising SAMs with EGaIn as top electrode and Au as bottom electrode. This value is also close to the experimentally measured value of E_{F} using UPS, detailed here in section 1.3.3 of SI. The use of this E_{F} value was also justified in the Figure 5 of the main text where the differences of the energies of HOPS and LUPS from the E_{F} value of EGaIn qualitatively reproduced the trend in the transition voltages obtained from the EGaIn experiments.

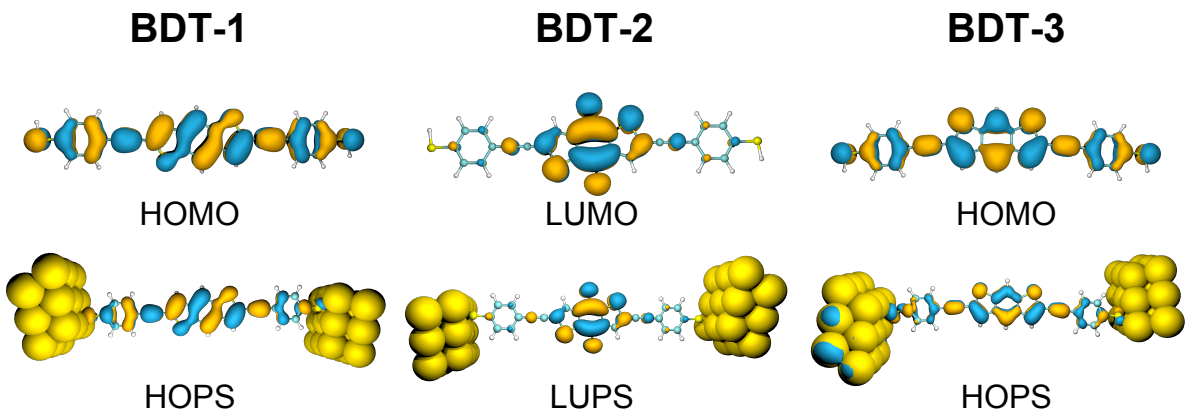

Figure S25: The figure compares the molecular orbitals (MOs) of the molecular systems in the gas-phase molecule and the molecule between electrode clusters. The figure only shows the MOs that contribute the most to the transmission, *i.e.*, HOPS for **BDT-**1 and **BDT-**3, and LUPS for **BDT-**2. The similarity in the shape and symmetry of different orbital pairs suggest that the electronic structure of the molecules is not perturbed by the electrodes.

References

(S1) Fracasso, D.; Valkenier, H.; Hummelen, J. C.; Solomon, G. C.; Chiechi, R. C. Evidence for Quantum Interference in SAMs of Arylethynylene Thiolates in Tunneling Junctions With Eutectic Ga-In (EGaIn) Top-Contacts. *J. Am. Chem. Soc.* **2011**, *133*, 9556–9563.

(S2) Guedon, C. M.; Valkenier, H.; Markussen, T.; Thygesen, K. S.; Hummelen, J. C.; Van Der Molen, S. J. Observation of Quantum Interference in Molecular Charge Transport. *Nat. Nanotechnol.* **2012**, *7*, 305–309.

(S3) Kaliginedi, V.; Moreno-García, P.; Valkenier, H.; Hong, W.; García-Suárez, V. M.; Buiter, P.; Otten, J. L. H.; Hummelen, J. C.; Lambert, C. J.; Wandlowski, T. Correlations Between Molecular Structure and Single-Junction Conductance: A Case Study With Oligo(phenylene-Ethynylene)-Type Wires. *J. Am. Chem. Soc.* **2012**, *134*, 5262–5275.

(S4) Hong, W.; Valkenier, H.; Mészáros, G.; Manrique, D. Z.; Mishchenko, A.; Putz, A.; García, P. M.; Lambert, C. J.; Hummelen, J. C.; Wandlowski, T. An MCBJ Case Study: The Influence of Π-Conjugation on the Single-Molecule Conductance at a Solid/Liquid Interface. *Beilstein J. Nanotechnol.* **2011**, *2*, 699–713.

(S5) Rabache, V.; Chaste, J.; Petit, P.; Della Rocca, M. L.; Martin, P.; Lacroix, J.-C.; McCreery, R. L.; Lafarge, P. Direct Observation of Large Quantum Interference Effect in Anthraquinone Solid-State Junctions. *J. Am. Chem. Soc.* **2013**, *135*, 10218–10221.

(S6) Carlotti, M.; Kovalchuk, A.; Wächter, T.; Qiu, X.; Zharnikov, M.; Chiechi, R. C. Conformation-Driven Quantum Interference Effects Mediated by Through-Space Conjugation in Self-Assembled Monolayers. *Nat. Commun.* **2016**, *7*, 13904.

(S7) Perrin, M. L.; Frisenda, R.; Koole, M.; Seldenthuis, J. S.; Celis, G. A.; Valkenier, H.; Hummelen, J. C.; Renaud, N.; Grozema, F. C.; Thijssen, J. M.; Dulić, D.; J., v. d.

Z. S. Large Negative Differential Conductance in Single-Molecule Break Junctions. *Nat. Nanotech.* **2014**, *9*, 830–834.

(S8) Borges, A.; Xia, J.; Liu, S. H.; Venkataraman, L.; Solomon, G. C. The Role of Through-Space Interactions in Modulating Constructive and Destructive Interference Effects in Benzene. *Nano Lett.* **2017**, *17*, 4436–4442.

(S9) Xia, J.; Capozzi, B.; Wei, S.; Strange, M.; Batra, A.; Moreno, J. R.; Amir, R. J.; Amir, E.; Solomon, G. C.; Venkataraman, L.; Campos, L. M. Breakdown of Interference Rules in Azulene, a Nonalternant Hydrocarbon. *Nano Lett.* **2014**, *14*, 2941–2945.

(S10) Yang, G.; Sangtarash, S.; Liu, Z.; Li, X.; Sadeghi, H.; Tan, Z.; Li, R.; Zheng, J.; Dong, X.; Liu, J.-Y.; Yang, Y.; Shi, J.; Xiao, Z.; Zhang, G.; Lambert, C.; wenjing Hong,; Zhang, D. Protonation Tuning of Quantum Interference in Azulene-Type Single-Molecule Junctions. *Chem. Sci.* **2017**, *8*, 7505–7509.

(S11) Mayor, M.; Weber, H. B.; Reichert, J.; Elbing, M.; von Hänisch, C.; Beckmann, D.; Fischer, M. Electric Current Through a Molecular Rod—Relevance of the Position of the Anchor Groups. *Angew. Chem., Int. Ed.* **2003**, *42*, 5834–5838.

(S12) Taniguchi, M.; Tsutsui, M.; Mogi, R.; Sugawara, T.; Tsuji, Y.; Yoshizawa, K.; Kawai, T. Dependence of Single-Molecule Conductance on Molecule Junction Symmetry. *J. Am. Chem. Soc.* **2011**, *133*, 11426–11429.

(S13) Meisner, J. S.; Ahn, S.; Aradhya, S. V.; Krikorian, M.; Parameswaran, R.; Steigerwald, M.; Venkataraman, L.; Nuckolls, C. Importance of Direct Metalπ Coupling in Electronic Transport Through Conjugated Single-Molecule Junctions. *J. Am. Chem. Soc.* **2012**, *134*, 20440–20445.

(S14) Arroyo, C. R.; Tarkuc, S.; Frisenda, R.; Seldenthuis, J. S.; Woerde, C. H. M.; Eelkema, R.; Grozema, F. C.; van der Zant, H. S. J. Signatures of Quantum Inter-

ference Effects on Charge Transport Through a Single Benzene Ring. *Angew. Chem., Int. Ed.* **2013**, *52*, 3152–3155.

(S15) Quinn, J. R.; Foss, F. W.; Venkataraman, L.; Hybertsen, M. S.; Breslow, R. Single-Molecule Junction Conductance Through Diaminoacenes. *J. Am. Chem. Soc.* **2007**, *129*, 6714–6715.

(S16) Kiguchi, M.; Nakamura, H.; Takahashi, Y.; Takahashi, T.; Ohto, T. Effect of Anchoring Group Position on Formation and Conductance of a Single Disubstituted Benzene Molecule Bridging Au Electrodes: Change of Conductive Molecular Orbital and Electron Pathway. *J. Phys. Chem. C* **2010**, *114*, 22254–22261.

(S17) Aradhya, S. V.; Meisner, J. S.; Krikorian, M.; Ahn, S.; Parameswaran, R.; Steigerwald, M. L.; Nuckolls, C.; Venkataraman, L. Dissecting Contact Mechanics From Quantum Interference in Single-Molecule Junctions of Stilbene Derivatives. *Nano Lett.* **2012**, *12*, 1643–1647.

(S18) Manrique, D. Z.; Huang, C.; Baghernejad, M.; Zhao, X.; Al-Owaedi, O. a.; Sadeghi, H.; Kaliginedi, V.; Hong, W.; Gulcur, M.; Wandlowski, T.; Bryce, M. R.; Lambert, C. J. A Quantum Circuit Rule for Interference Effects in Single-Molecule Electrical Junctions. *Nat. Commun.* **2015**, *6*, 6389.

(S19) Gantenbein, M.; Wang, L.; Al-jobory, A. A.; Ismael, A. K.; Lambert, C. J.; Bryce, M. R. Quantum Interference and Heteroaromaticity of Para- And Meta-Linked Bridged Biphenyl Units in Single Molecular Conductance Measurements. *Sci. Rep.* **2017**, *7*, 1794.

(S20) Kuo, C.-Y.; Nie, W.; Tsai, H.; Yen, H.-J.; Mohite, A. D.; Gupta, G.; Dattelbaum, A. M.; William, D. J.; Cha, K. C.; Yang, Y.; Wang, L.; Wang, H.-L. Structural Design of Benzo[1,2-B:4,5-B]dithiophene-Based 2D Conjugated Polymers With

Bithienyl and Terthienyl Substituents Toward Photovoltaic Applications. *Macromolecules* **2014**, *47*, 1008–1020.

(S21) Rieger, R.; Beckmann, D.; Mavrinskiy, A.; Kastler, M.; Müllen, K. Backbone Curvature in Polythiophenes. *Chem. Mater.* **2010**, *22*, 5314–5318.

(S22) Shi, Z.-F.; Wang, L.-J.; Wang, H.; Cao, X.-P.; Zhang, H.-L. Synthesis of Oligo(phenylene Ethynylene)s With Dendrimer "Shells" for Molecular Electronics. *Org. Lett.* **2007**, *9*, 595–598.

(S23) van Dijk, E. H.; Myles, D. J. T.; van der Veen, M. H.; Hummelen, J. C. Synthesis and Properties of an Anthraquinone-Based Redox Switch for Molecular Electronics. *Org. Lett.* **2006**, *8*, 2333–2336.

(S24) Pijper, T. C.; Robertus, J.; Browne, W. R.; Feringa, B. L. Mild Ti-Mediated Transformation of T-Butyl Thio-Ethers Into Thio-Acetates. *Org. Biomol. Chem.* **2015**, *13*, 265–268.

(S25) Valkenier, H.; Huisman, E. H.; van Hal, P. A.; de Leeuw, D. M.; Chiechi, R. C.; Hummelen, J. C. Formation of High-Quality Self-Assembled Monolayers of Conjugated Dithiols on Gold: Base Matters. *J. Am. Chem. Soc.* **2011**, *133*, 4930–4939.

(S26) Weiss, E. A.; Kaufman, G. K.; Kriebel, J. K.; Li, Z.; Schalek, R.; Whitesides, G. M. Si/SiO2-Templated Formation of Ultraflat Metal Surfaces on Glass, Polymer, and Solder Supports: Their Use as Substrates for Self-Assembled Monolayers. *Langmuir* **2007**, *23*, 9686–9694.

(S27) Carlotti, M.; Degen, M.; Zhang, Y.; Chiechi, R. C. Pronounced Environmental Effects on Injection Currents in EGaIn Tunneling Junctions Comprising Self-Assembled Monolayers. *J. Phys. Chem. C* **2016**, *120*, 20437–20445.

(S28) Valkenier, H.; Guedon, C. M.; Markussen, T.; Thygesen, K. S.; van der Molen, S. J.; Hummelen, J. C. Cross-Conjugation and Quantum Interference: A General Correlation? *Phys. Chem. Chem. Phys.* **2014**, *16*, 653–662.

(S29) Nefedov, A.; Wöll, C. Advanced Applications of NEXAFS Spectroscopy for Functionalized Surfaces. *Surface Science Techniques* **2013**,

(S30) D. Briggs,; C. D. Wanger,; W. M. Riggs,; L. E. Davis,; J. F. Moulder,; G. E.Muilenberg, *Handbook of X-Ray Photoelectron Spectroscopy*; Heyden & Son Ltd.: Perkin-Elmer Corp., Physical Electronics Division, Eden Prairie, Minnesota, USA, 1981; Vol. 3; pp 190–195.

(S31) Thome, J.; Himmelhaus, M.; Zharnikov, M.; Grunze, M. Increased Lateral Density in Alkanethiolate Films on Gold by Mercury Adsorption. *Langmuir* **1998**, *14*, 7435–7449.

(S32) Ratner, B. D.; Castner, D. G. *Surface Analysis - The Principal Techniques*; John Wiley & Sons, Ltd, 1997; pp 47–112.

(S33) Lamont, C. L. A.; Wilkes, J. Attenuation Length of Electrons in Self-Assembled Monolayers of N-Alkanethiols on Gold. *Langmuir* **1999**, *15*, 2037–2042.

(S34) Abu-Husein, T.; Schuster, S.; Egger, D. A.; Kind, M.; Santowski, T.; Wiesner, A.; Chiechi, R. C.; Zojer, E.; Terfort, A.; Zharnikov, M. The Effects of Embedded Dipoles in Aromatic Self-Assembled Monolayers. *Adv. Funct. Mater.* **2015**, *25*, 3943–3957.

(S35) Schreiber, F. Structure and Growth of Self-Assembling Monolayers. *Prog. Surf. Sci.* **2000**, *65*, 151–257.

(S36) Stohr, J. *NEXAFS Spectroscopy*; Springer-Verlag Berlin Heidelberg, 1992.

(S37) Batson, P. E. Carbon 1s Near-Edge-Absorption Fine Structure in Graphite. *Phys. Rev. B* **1993**, *48*, 2608–2610.

(S38) Joshua J Stapleton,; Philipp Harder,; Thomas A Daniel,; Michael D Reinard,; Yuxing Yao,; David W Price,; James M Tour,; David L Allara, Self-Assembled Oligo(phenylene-Ethynylene) Molecular Electronic Switch Monolayers on Gold: Structures and Chemical Stability. *Langmuir* **2003**, *19*, 8245–8255.

(S39) Nilsson, D.; Watcharinyanon, S.; Eng, M.; Li, L.; Moons, E.; Johansson, L. S. O.; Zharnikov, M.; Shaporenko, A.; Albinsson, B.; Må rtensson, J. Characterization of Self-Assembled Monolayers of Oligo(phenyleneethynylene) Derivatives of Varying Shapes on Gold: Effect of Laterally Extended Π-Systems. *Langmuir* **2007**, *23*, 6170–6181.

(S40) Hamoudi, H.; Kao, P.; Nefedov, A.; Allara, D. L.; Zharnikov, M. X-Ray Spectroscopy Characterization of Self-Assembled Monolayers of Nitrile-Substituted Oligo(phenylene Ethynylene)s With Variable Chain Length. *Beilstein J. Nanotechnol.* **2012**, *3*, 12–24.

(S41) Frey, S.; Stadler, V.; Heister, K.; Eck, W.; Zharnikov, M.; Grunze, M.; Zeysing, B.; Terfort, A. Structure of Thioaromatic Self-Assembled Monolayers on Gold and Silver. *Langmuir* **2001**, *17*, 2408–2415.

(S42) Zharnikov, M. High-Resolution X-Ray Photoelectron Spectroscopy in Studies of Self-Assembled Organic Monolayers. *J. Electron Spectrosc. Relat. Phenom.* **2010**, *178–179*, 380–393.

(S43) Sako, E. O.; Kondoh, H.; Nakai, I.; Nambu, A.; Nakamura, T.; Ohta, T. Reactive Adsorption of Thiophene on Au(111) From Solution. *Chem. Phys. Lett.* **2005**, *413*, 267–271.

(S44) Tai, Y.; Shaporenko, A.; Rong, H.-T.; Buck, M.; Eck, W.; Grunze, M.; Zharnikov, M. Fabrication of Thiol-Terminated Surfaces Using Aromatic Self-Assembled Monolayers. *J. Phys. Chem. B* **2004**, *108*, 16806–16810.

(S45) Heister, K.; Frey, S.; Ulman, A.; Grunze, M.; Zharnikov, M. Irradiation Sensitivity of Self-Assembled Monolayers With an Introduced "Weak Link". *Langmuir* **2004**, *20*, 1222–1227.

(S46) Shaporenko, A.; Adlkofer, K.; Johansson, L.; Tanaka, M. Functionalization of GaAs Surfaces With Aromatic Self-Assembled Monolayers: A Synchrotron-Based Spectroscopic Study. *Langmuir* **2003**,

(S47) Neese, F. The ORCA Program System. *Wiley Interdiscip. Rev.: Comput. Mol. Sci.* **2012**, *2*, 73–78.

(S48) Neese, F. Software update: the ORCA program system, version 4.0. *Wiley Interdisciplinary Reviews: Computational Molecular Science*

(S49) Herrmann, C.; Gross, L.; Steenbock, T.; Deffner, M.; Voigt, B. A.; Solomon, G. C. ARTAIOS - A Transport Code for Postprocessing Quantum Chemical Electronic Structure Calculations, Available From https://www.chemie.uni-hamburg.de/ac/herrmann/software/index.html. 2016.

(S50) Herrmann, C.; Solomon, G. C.; Subotnik, J. E.; Mujica, V.; Ratner, M. A. Ghost Transmission: How Large Basis Sets Can Make Electron Transport Calculations Worse. *J. Chem. Phys.* **2010**, *132*, 024103.

(S51) Weigend, F.; Ahlrichs, R. Balanced Basis Sets of Split Valence{,} Triple Zeta Valence and Quadruple Zeta Valence Quality for H to Rn: Design and Assessment of Accuracy. *Phys. Chem. Chem. Phys.* **2005**, *7*, 3297–3305.

(S52) Gold-Palladium Electrocatalysts. *Electrochim. Acta* **1967**, *12*, 579–581.

(S53) Schlicke, H.; Herrmann, C. Controlling Molecular Conductance: Switching Off Sites Through Protonation. *ChemPhysChem* **2014**, *15*, 4011–4018.

(S54) Bilić, A.; Reimers, J. R.; Hush, N. S. The Structure, Energetics, and Nature of the Chemical Bonding of Phenylthiol Adsorbed on the Au(111) Surface: Implications for Density-Functional Calculations of Molecular-Electronic Conduction. *J. Chem. Phys.* **2005**, *122*, 094708.

(S55) Nerngchamnong, N.; Yuan, L.; Qi, D.-C.; Li, J.; Thompson, D.; Nijhuis, C. a. The Role of Van Der Waals Forces in the Performance of Molecular Diodes. *Nat. Nanotechnol.* **2013**, *8*, 113–118.

(S56) Cabarcos, O. M.; Schuster, S.; Hehn, I.; Zhang, P. P.; Maitani, M. M.; Sullivan, N.; Gigure, J.-B.; Morin, J.-F.; Weiss, P. S.; Zojer, E.; Zharnikov, M.; Allara, D. L. Effects of Embedded Dipole Layers on Electrostatic Properties of Alkanethiolate Self-Assembled Monolayers. *The Journal of Physical Chemistry C* **2017**, *121*, 15815–15830.

(S57) Kovalchuk, A.; Abu-Husein, T.; Fracasso, D.; Egger, D. A.; Zojer, E.; Zharnikov, M.; Terfort, A.; Chiechi, R. C. Transition voltages respond to synthetic reorientation of embedded dipoles in self-assembled monolayers. *Chem. Sci.* **2016**, *7*, 781–787.

(S58) AbuHusein, T.; Schuster, S.; Egger, D. A.; Kind, M.; Santowski, T.; Wiesner, A.; Chiechi, R.; Zojer, E.; Terfort, A.; Zharnikov, M. The Effects of Embedded Dipoles in Aromatic SelfAssembled Monolayers. *Advanced Functional Materials 25*, 3943–3957.